Available online at www.sciencedirect.com
SCIENCE DIRECT®
Fusion Engineering and Design 72 (2004) 63–81
Fusion Engineering and Design
www.elsevier.com/locate/fusengdes

Thermofluid modeling and experiments for free surface flows of low-conductivity fluid in fusion systems

S. Smolentsev[a,*], N. Morley[a], B. Freeze[a], R. Miraghaie[a], J.-C. Nave[b], S. Banerjee[b], A. Ying[a], M. Abdou[a]

[a] *UCLA, MAE Department, 44-114 Engineering IV, 420 Westwood Pza, Los Angeles, CA 90095-1597, USA*
[b] *UCSB, ME Department, Santa Barbara, CA 93106, USA*

Available online 11 September 2004

Abstract

The paper summarizes results of experimental and theoretical studies related to the flow of liquids with a free surface and poor electrical and thermal conductivity, such as molten salts, under conditions relevant to fusion energy systems. These results have been obtained over last several years when developing the liquid wall concept as a part of the APEX project [M.A. Abdou, The APEX TEAM, On the exploration of innovative concepts for fusion chamber technology, Fusion Eng. Des. 54 (2001) 181–247]. As a theoretical tool a modified K–ε model of turbulence coupled with the Navier–Stokes equations written in the thin-shear-layer approximation is used for studying wavy, turbulent flows in a spanwise magnetic field. The experimental part covers current results for supercritical flows in regimes transitional from "weak" to "strong" turbulence, which are expected to occur in the reference liquid wall flows. The paper also describes on-going work on novel schemes of heat transfer promotion and current directions for direct numerical simulation.

Keywords: Turbulence; Free surface; Surface waves; Heat transfer; Magnetohydrodynamics; APEX

1. Introduction

The APEX (advanced power extraction) study [1] has focused a significant amount of attention on the possibility of utilizing flowing liquid layers as a virtual First Wall in magnetic fusion reactors. Such a concept requires that the liquid layer absorbs energy from the plasma in the form of radiation and energetic charged and neutral particles. As a particular design that can potentially accommodate such First Wall heat loads utilizing a molten salt as the working liquid, we will refer to the CLiFF concept detailed in [2]. In CLiFF, the molten salt flows poloidally over the reactor First Wall from the chamber top to bottom, forming a liquid layer with a thickness of about 2 cm, and the velocity of about 10 m/s. The free surface in the CLiFF flows is exposed to a high surface heat flux ($\sim$2 MW/m^2) from the surrounding plasma and is affected by a strong reactor magnetic field ($\sim$10 T). A key thermofluid issue for molten salt flows under CLiFF parameters is the minimization of the surface temperature, and thus the amount of evaporated material that could potentially

* Corresponding author. Tel.: +1 310 794 5366; fax: +1 310 825 2599.
E-mail address: sergey@fusion.ucla.edu (S. Smolentsev).

0920-3796/$ – see front matter © 2004 Elsevier B.V. All rights reserved.
doi:10.1016/j.fusengdes.2004.07.003

enter and poison the plasma. This surface temperature will be critically related to the heat transfer at the free interface facing the plasma heat flux.

For many years high heat capacity, high thermal/electrical conductivity media such as liquid metals have been studied as possible coolants for fusion reactors. Molten salt flow and heat transfer differs from liquid metals in critical ways. Molten salts typically have low thermal conductivity and so heat transfer through the flow is highly dependent on the level of turbulence. This is not true for liquid metals that have very high thermal conduction. Near the free surface this turbulent transport process is known as surface renewal [3]—where cooler (warmer) liquid from the flow bulk (free surface) is delivered to the free surface (flow bulk) by the turbulent structures. The turbulence motion itself will be affected both by the proximity of the interface and the strength of the magnetic field.

Turbulent structures in the flow undergo redistribution near a free surface [4], where the normal velocity component is strongly constrained by the free surface tension and the gravity force. This effect results in a near-surface "blockage" layer with thickness in the order of the typical turbulence scale [5] where the heat transport can be significantly reduced in comparison with the flow bulk. The turbulence redistribution process, however, can be strongly influenced by any wave phenomena—an essential part of free surface flows. Under CLiFF conditions, surface waves are mostly generated through deforming the free surface by the turbulent structures from the flow bulk.

Turbulent flow behavior will also be affected by the interaction with the magnetic field. Liquid metals, due to their high electrical conductivity ($\sim 10^6\ \Omega^{-1}\ \mathrm{m}^{-1}$), have strong magnetohydrodynamic (MHD) interaction when flowing across the reactor magnetic field that can result in an excessive MHD drag, as well as turbulence suppression. Based on the experimental data [6], the laminarization in liquid metal closed channel flows occurs if $Ha/Re > [Ha/Re]_{\mathrm{cr}}$. The Hartmann number, $Ha = B_0 l\sqrt{\sigma/(\nu\rho)}$, and the Reynolds number, $Re = U_{\mathrm{m}} l/\nu$, are built using the applied magnetic field (B_0), bulk mean velocity (U_{m}), characteristic flow dimension (l), and physical properties of fluid: electrical conductivity (σ), kinematic viscosity (ν), and density (ρ). Unlike liquid metals, molten salts have a much lower electrical conductivity ($\sim 10^2\ \Omega^{-1}\ \mathrm{m}^{-1}$) and do not experience such strong MHD forces and to a large extent remain turbulent ($Ha/Re < [Ha/Re]_{\mathrm{cr}}$). But the turbulence may be modified and partially suppressed by interaction with the magnetic field when compared to flows of non-conducting liquids. The suppression of turbulence is caused by the damping effect arising from dissipation of the turbulent kinetic energy into the Joule heat. Suppressing the turbulence pulsations by the magnetic field results in reduction of the effective thermal conductivity across the interface.

The primary goal of the present study is to give a detailed description of the thermofluid phenomena in the near-surface region of a turbulent free surface flow in a magnetic field under conditions relevant to fusion systems. The considerations are based on the experimental and theoretical studies, which were conducted over last several years when working on the APEX project. Some technical results have already been presented in the earlier publications [7,8]. The present paper is primary intended to emphasize practical aspects of using the theory developed when applying it to fusion related problems. All the results are presented in the paper in the following way. Following the present introductory section, Section 2 gives a general description of the extended K–ε model including governing equations, boundary conditions and turbulence closures. The experimental results and validations of the model along with the evaluations for the turbulent Prandtl number are presented in Section 3. Examples of application of the model to the CLiFF flows and heat transfer are given in Section 4. Section 5 introduces novel approaches for heat transfer enhancement in open surface flows and explains preliminary experimental results on improving heat transfer through changes of the back-wall topology. The paper also illustrates some results on free surface deformations in free falling films, which were calculated numerically by means of direct numerical simulation (DNS) in Section 6. Section 7 summarizes the most important results.

2. K–ε model as a tool for studying thermofluid phenomena in fusion systems

The turbulence models are many in number and differ in many ways depending on their range of applicability, level of closure and mathematical complexity [9]. In the present study, we use the K–ε model developed in [7] as a basic theoretical tool for studying

thermofluid phenomena under CLiFF type conditions. Unlike standard two-equation models [9], which are not directly applied to MHD flows, the present one had been adjusted by using experimental data for electrically conducting fluid flows in a magnetic field perpendicular to the main flow direction. As applied to the fusion systems, this case represents poloidal flows in a toroidal reactor magnetic field. In this section we briefly describe the model and modified free surface boundary conditions that extend non-MHD boundary conditions originally proposed in [10]. The effect of a free surface on heat transfer is incorporated through the turbulent Prandtl number, which was adjusted using the experimental data.

2.1. Turbulence closure for the electromagnetic terms

The starting point for the development of a turbulence model is the standard set of the flow equations for incompressible liquids, known as the Navier–Stokes equations, along with the energy equation and equations for electromagnetic quantities known as the Maxwell equations [6]. The turbulent flows can be analyzed by using these equations through the so-called Reynolds decomposition [9], i.e. dividing the flow and other parameters into mean and fluctuating parts. For example, the velocity field is decomposed in the following way:

$$v_j = \langle v_j \rangle + v'_j,$$

where $\langle v_j \rangle$ is the mean and v'_j the fluctuating part. After decomposing, the equations are averaged in the long time or ensemble average sense. The new equations obtained resemble the laminar equations. However, some new terms appear, which consist of correlations between various fluctuating components. In the momentum equation, the new terms appear as stress terms denoted as the Reynolds stresses: $R_{ij} = -\rho\langle v'_i v'_j \rangle$. In the energy equation, the new term has the form of a turbulent heat flux, such as $\langle t' v'_j \rangle$. In order to get a closed set of equations, these new unknowns need to be modeled. The corresponding closures are often constructed by introducing a so-called turbulent viscosity (eddy viscosity or eddy diffusivity for momentum), ν_t. Unlike the molecular viscosity, ν_t is not a physical property and can vary widely both in time and space. Another, closure parameter is the turbulent Prandtl number, Pr_t, which expresses the ratio of the eddy diffusivity for momentum to the eddy diffusivity for heat. In terms of ν_t and Pr_t, the turbulent shear stress and heat flux in a boundary-layer type flow can be described as

$$\langle u' v' \rangle = -\nu_t \frac{\partial U}{\partial y}, \tag{1a}$$

$$\langle t' v' \rangle = -\frac{\nu_t}{Pr_t} \frac{\partial T}{\partial y}. \tag{1b}$$

Assuming low magnetic Reynolds number ($Re_m = \mu\sigma l U_m \ll 1$, where μ is the magnetic permeability and the other symbols as described above) and applying Reynolds averaging to the Navier–Stokes–Maxwell equations with the conventional closure approximations, one can obtain equations for the turbulent kinetic energy per unit mass, K, and the dissipation rate per unit mass, ε. Once these two quantities are known, the eddy viscosity can be calculated by using the so-called Kolmogorov–Prandtl expression:

$$\nu_t = \frac{C_\nu K^2}{\varepsilon}$$

with C_ν as a model coefficient. The transport equation for K is derived here by the conventional method. After decomposing the velocity into the mean and fluctuating parts, each of the equations for the fluctuating parts is multiplied by the corresponding pulsation velocity component. Then, the equations obtained are added together and averaged. Finally, unknown turbulent correlations are replaced by algebraic expressions with closure coefficients. Doing all these steps results in the equation for K as follows:

$$\frac{\partial K}{\partial t} + \langle v_j \rangle \frac{\partial K}{\partial x_j} = \underbrace{\nu_t \left(\frac{\partial \langle v_j \rangle}{\partial x_j} \right)^2}_{\text{Production}} + \underbrace{\frac{\partial}{\partial x_j} \left[\left(\nu + \frac{\nu_t}{\sigma_K} \right) \frac{\partial K}{\partial x_j} \right]}_{\text{Diffusion}} - \underbrace{\varepsilon - \varepsilon^K_{\text{em}}}_{\text{Dissipation}}. \tag{2}$$

The first three terms on the RHS of Eq. (2) are standard, while the fourth one, $\varepsilon^K_{\text{em}}$, is electromagnetic. The expression for $\varepsilon^K_{\text{em}}$ is obtained by the above procedure and comes from the Lorentz force term on the RHS of the momentum equation for the fluctuating velocity as

follows:

$$\varepsilon^K_{\rm em} = D_{\rm I} + D_{\rm II} = \underbrace{\frac{\sigma}{\rho}(2B_0^2 K - B_{0i}B_{0k}\langle v_i' v_k'\rangle)}_{D_{\rm I}} + \underbrace{\frac{\sigma}{\rho}\varepsilon_{ijk}B_{0k}\left\langle \frac{\partial\varphi'}{\partial x_j} v_i' \right\rangle}_{D_{\rm II}}, \quad (3)$$

where ε_{ijk} is the Levi-Civita symbol defined by

$$\varepsilon_{ijk} = \begin{cases} +1 \text{ if } (i, j, k) \text{ are cyclic,} \\ -1 \text{ if } (i, j, k) \text{ are anticyclic,} \\ 0 \text{ otherwise.} \end{cases}$$

Here, $B_0 = \left(\sqrt{B_{01}^2 + B_{02}^2 + B_{03}^2}\right)$ is the applied magnetic field, and φ the electric potential, which is also decomposed into the mean and fluctuating parts, such that $\varphi = \langle\varphi\rangle + \varphi'$. The exact equation for ε can also be derived. However, following the general practice, the standard model equation for ε is best viewed as being entirely empirical [11]:

$$\frac{\partial\varepsilon}{\partial t} + \langle v_j\rangle\frac{\partial\varepsilon}{\partial x_j} = C_1\frac{\varepsilon}{K}\nu_{\rm t}\left(\frac{\partial\langle v_i\rangle}{\partial x_j}\right)^2 + \frac{\partial}{\partial x_j}\left[\left(\nu + \frac{\nu_{\rm t}}{\sigma_\varepsilon}\right)\frac{\partial\varepsilon}{\partial x_j}\right] - C_2\frac{\varepsilon}{K}\varepsilon - \varepsilon^\varepsilon_{\rm em}. \quad (4)$$

In Eqs. (2) and (4), C_1, C_2, σ_K, and σ_ε are the conventional closure coefficients. Similar to Eq. (2), Eq. (4) also includes the electromagnetic term, $\varepsilon^\varepsilon_{\rm em}$, which is not necessarily the same as that in (2). The production term in both equations is given in a simplified form, which is appropriate for channel flows. The essence of the turbulence model is how to model the electromagnetic terms. The analysis of the sink term, $\varepsilon^K_{\rm em}$, and the closure relation for it are given below. In modeling the destruction term, $\varepsilon^\varepsilon_{\rm em}$, we used the commonly accepted approach (see [12,13]), whereby the closure form for this term is adopted from that for $\varepsilon^K_{\rm em}$.

Expression (3) includes two terms, $D_{\rm I}$ and $D_{\rm II}$, which come from two components in Ohm's law: $\sigma\boldsymbol{V}' \times \boldsymbol{B}_0$ and $-\sigma\nabla\varphi'$, respectively. The term $D_{\rm I}$ is always positive, while $D_{\rm II}$ is negative. Although the ratio between $D_{\rm I}$ and $D_{\rm II}$ can vary in a wide range depending on the flow parameters, their sum, $\varepsilon^K_{\rm em}$, which stands for the Joule dissipation, is always positive. In what follows, we will restrict ourselves to examine the effect of a one-component magnetic field, which is assumed to be perpendicular to the main flow direction. This includes both the wall-normal and spanwise orientations of the magnetic field with respect to the main flow. Table 1 gives $D_{\rm I}$ and $D_{\rm II}$ for these particular cases. In the table and below, x, y, z and u', v', w' denote the Cartesian coordinates and corresponding pulsating velocity components. The main flow is assumed to be in the x-axis direction.

To model $\varepsilon^K_{\rm em}$ one can draw on the following generally observed tendency [14]. The distribution of $D_{\rm II}$ is similar in shape to that of $D_{\rm I}$ and both are similar in shape to the distribution of K. This gives a ground to model $\varepsilon^K_{\rm em}$ in the following form:

$$\varepsilon^K_{\rm em} = C_3\frac{\sigma}{\rho}B_0^2 K,$$

and then to adopt the following expression for $\varepsilon^\varepsilon_{\rm em}$:

$$\varepsilon^\varepsilon_{\rm em} = C_4\frac{\sigma}{\rho}B_0^2\varepsilon,$$

where C_3 and C_4 are additional closure coefficients. In channel flows with a weak magnetic field ($Ha/Re \ll (Ha/Re)_{\rm cr}$), the turbulence structure is close to that in ordinary flows where streamwise vortices dominate. For such flows, the Joule dissipation is mostly contributed by $D_{\rm I}$. Taking into account that $\langle v'v'\rangle, \langle w'w'\rangle < \langle u'u'\rangle$ and $2K = \langle u'u'\rangle + \langle v'v'\rangle + \langle w'w'\rangle$ one can arrive at $C_3 \approx 2$. In the opposite particular case of a strong magnetic field, transition

Table 1
Specification of electromagnetic term $\varepsilon^K_{\rm em}$ for a one-component magnetic field

B_0	$D_{\rm I}$	$D_{\rm II}$
$(0, B_{0y}, 0)$ (wall-normal)	$\frac{\sigma}{\rho}B_{0y}^2(\langle u'u'\rangle + \langle w'w'\rangle)$	$\frac{\sigma}{\rho}B_{0y}\left(\left\langle\frac{\partial\varphi'}{\partial x}w'\right\rangle - \left\langle\frac{\partial\varphi'}{\partial z}u'\right\rangle\right)$
$(0, 0, B_{0z})$ (spanwise)	$\frac{\sigma}{\rho}B_{0z}^2(\langle u'u'\rangle + \langle v'v'\rangle)$	$\frac{\sigma}{\rho}B_{0z}\left(\left\langle\frac{\partial\varphi'}{\partial y}u'\right\rangle - \left\langle\frac{\partial\varphi'}{\partial x}v'\right\rangle\right)$

Table 2
Specification of the electromagnetic terms in equations for K and ε after modeling for closed channel flows

Magnetic field direction	ε^K_{em}	$\varepsilon^\varepsilon_{em}$	C_3	C_4	Experimental data used
Spanwise	$C_3 \frac{\sigma}{\rho} B_0^2 K$	$C_4 \frac{\sigma}{\rho} B_0^2 \varepsilon$	$1.9\ \exp\{-1.0N\}$	$1.9\ \exp\{-2.0N\}$	[16]
Wall-normal	$C_3 \frac{\sigma}{\rho} B_0^2 K$	$C_4 \frac{\sigma}{\rho} B_0^2 \varepsilon$	$1.9\ \exp\{-1.0N\}$	$1.9\ \exp\{-2.0N\}$	[17]

The interaction parameter, N, is build through the channel width.

to a 2D state occurs, in which turbulent eddies are elongated in the field direction, so that D_{I} and D_{II} become nearly equal in magnitude but opposite in sign, and $\varepsilon^K_{em} \to 0$. Therefore C_3 drops from about 2 to a smaller value as the magnetic field grows. In the present study, we adopt an exponential approximation for C_3 similar to that in [15] for pipe MHD flows, where it was suggested in the following form:

$$C_3 \sim \exp\{-N\},$$

where $N = Ha^2/Re$ is the interaction parameter, which characterize the ratio of electromagnetic to inertia forces. However, the details of implementation of the present model and the numerical values of closure parameters are different from those given in [15]. The present evaluations of the closure parameters have been developed using well-documented sets of the experimental data for the friction factor, c_f, in MHD flows in slotted channels [16,17] and are summarized in Table 2.

Figs. 1 and 2 illustrate the accuracy of evaluating the closure parameters in the electromagnetic terms, by comparing the calculated friction factor with the experimental data. As it can be seen from Table 2, the same model specification can be used for two orientations. However, using the same closure constants does not automatically mean the same degree of turbulence suppression. In the wall-normal field case, the magnetic field has a stronger effect, which is explained by flattening the velocity profile due to the Hartmann effect.

Since the mechanism of turbulence suppression by a magnetic field in open and closed channel flows is of the same nature, the same closure terms can be used when modeling open channel flows, but with some modifications in the numerical values:

$$C_3 = 1.9\ \exp\{-2.0N\}, \qquad C_4 = 1.9\ \exp\{-4.0N\},$$

where the interaction parameter is build through the flow thickness, h. Doubling the power in comparison with the closed channels is introduced because from the geometrical viewpoint, the open channel flow with the depth h can be treated as a half of the closed channel flow with the width $2h$. More detailed description of the turbulence closure for the electromagnetic terms including an additional case of the streamwise orientation of the applied magnetic field can be found in [7].

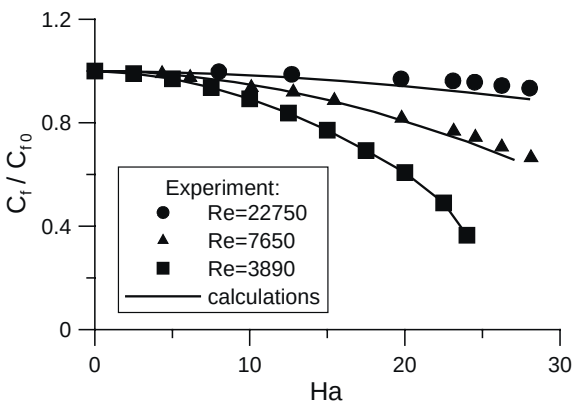

Fig. 1. Experimental [16] and calculated friction factor in closed channel flow for a spanwise magnetic field.

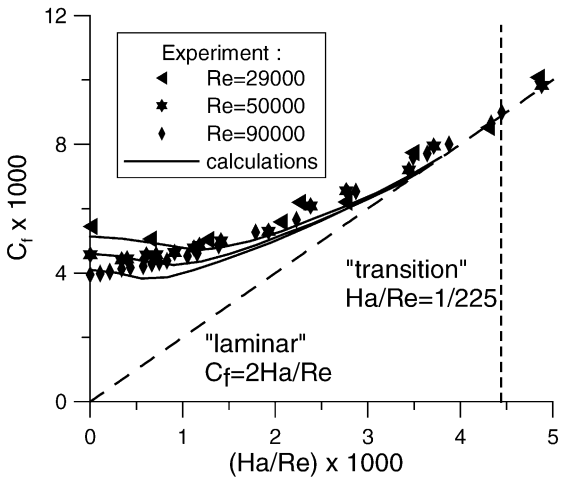

Fig. 2. Experimental [17] and calculated friction factor results for a wall-normal magnetic field.

2.2. Free surface boundary conditions

In the first studies of turbulent flows in open channels, the "rigid-lid" surface was assumed to act like a plane of symmetry. The symmetry condition requires that both K and ε have zero surface-normal gradient at the surface:

$$\left(\frac{\partial K}{\partial y}\right)_s = 0, \qquad \left(\frac{\partial \varepsilon}{\partial y}\right)_s = 0. \tag{5}$$

However, using such conditions results in overestimated values for K and ν_t near the surface. More physical free surface boundary condition based on the experimental data were proposed by Hossain and Rodi [10]:

$$\left(\frac{\partial K}{\partial y}\right)_s = 0, \qquad \varepsilon_s = \frac{C_\nu^{3/4} K_s^{3/2}}{0.07h\kappa}. \tag{6}$$

The second condition of (6) expresses the empirical fact that the dissipation length scale at the free surface of non-wavy flows has been observed to be about 7% of the flow thickness:

$$l_s = 0.07h, \tag{7}$$

where l is defined as $l = C_\nu^{3/4} K^{3/2} \varepsilon^{-1} \kappa^{-1}$ and κ is the von Karman constant. It should be noted that recent DNS data for non-wavy flows [26] show a different tendency. Namely, l_s grows when approaching the free surface. Using these DNS data in the model may improve its quality. However, here we rely on the empirical formula (7) and boundary condition (6), which give a well-known "parabolic" distribution of ν_t with the maximum at about halfway between the wall and the free surface. Also, with this boundary condition the calculated mean flow thickness agrees very well with the experimental data for flows with a moderate waviness (see Section 3.4). However, a magnetic field rapidly changes the dissipation length scale, so that (7) is applicable only in a very low field. One can expect shortening l_s as the field grows. To incorporate MHD effects in the boundary conditions we used the following modification of (6). First, two new quantities, l_{s1} and l_{s0}, are calculated as the dissipation length scales at the free surface with and without a magnetic field, respectively, using the symmetry boundary condition (5). Then, modified l_s is introduced in (6) in the form of $l_s = 0.07h \times l_{s1}/l_{s0}$ that results in

$$\left(\frac{\partial K}{\partial y}\right)_s = 0, \qquad \varepsilon_s = \frac{C_\nu^{3/4} K_s^{3/2}}{0.07h\kappa} \frac{l_{s0}}{l_{s1}}. \tag{8}$$

After that, the flow calculations can be repeated with the new boundary conditions. However, in a strong magnetic field, flow laminarization occurs. First, the flow becomes laminirized near the free surface, where the turbulence production is much lower than that near the solid wall. For such flows boundary conditions (8) are not applicable any more, and better boundary conditions are given by (5). Based on the calculations [7], the symmetry boundary condition could be recommended if the parameter Ha/Re exceeds 2.0×10^{-3} and 8.0×10^{-4} for a spanwise and wall-normal magnetic field, respectively. For comparison, $[Ha/Re]_{cr}$ at which flow laminarization occurs in closed channel flows in the whole area for these cases is 8.0×10^{-3} [16] and 4.5×10^{-3} [17], respectively.

2.3. Effect of free surface on heat transfer

There are several physical mechanisms at the free surface, which affect the heat transfer rate across the interface. First, the turbulence redistribution in the free surface region occurs. There has been much experimental and numerical evidence of the turbulent structure change in this region. The velocity pulsations normal to the surface are suppressed due to the joint action of the capillary forces and gravity, while the other two components are enhanced due to the mass conservation [4,6,14]. Hence, in the presence of a free surface, 3D bulk turbulence degenerates into a specific surface turbulence, in which turbulent vortices tend to be attached to the surface. Such vortices are two-dimensional at the surface (the rotation occurs in the free surface plane) and do not enhance heat transfer. It leads one to speak about near-surface flow laminarization in sense of heat transfer degradation. At the same time, turbulence eddies in the flow bulk almost do not undergo any structural changes. This fact means that the thermal resistance is not uniform across the flow and grows in the free surface region reaching its maximum at the surface. However, heat transfer improvement is also possible through turbulent mixing at the surface due to the surface renewal mechanism or by the surface waves. All these mechanisms introduce an anisotropy in the

distribution of turbulence. The K–ε model cannot describe properly the flow anisotropy, since the model does not take into consideration the individual components of the turbulence kinetic energy. However, in terms of heat transfer, implementing the anisotropy effect on heat transport is possible by modifying some parameters entering the energy equation.

In turbulence modeling of heat transport, the commonly accepted model for the averaged turbulent flux is given by the extension of the Fourier law for the heat conduction:

$$\langle t' v'_j \rangle = -\frac{\nu_t}{Pr_t}\frac{\partial T}{\partial x_j}. \quad (9)$$

The distribution of the eddy viscosity in (9) is responsible for changes of the turbulence level across the layer and thus incorporates the stabilizing effect of a magnetic field as well as reduction of turbulence and turbulent heat transfer at the free surface. The other parameter in formula (9), the turbulent Prandtl number (Pr_t), if properly adjusted, introduces the anisotropy effect. The turbulent Prandtl number stands for the ratio between the eddy diffusivity for momentum and eddy diffusivity for heat. For isotropic flows, this parameter is close to unity. This fact has been known as the "Reynolds analogy". The Reynolds analogy is obeyed very well in the bulk of the closed channel flows. However, this analogy is inappropriate in the near-surface vicinity, where the heat transfer rate is sufficiently poorer. To describe properly heat transfer degradation in the free surface region, Pr_t should be evaluated from experimental data. In the present study, the evaluation of this parameter was performed using the experimental data for flows with and without surface waves that represent different flow regimes relevant to the fusion systems. These evaluations are presented in the subsequent sections.

3. Experimental results and validation of the model predictions

The experiments with inclined open surface water flows heated from the free surface were performed to specify the range of applicability of the K–ε model as a tool for calculating hydrodynamic quantities, such as the mean flow thickness, and also to validate its adequacy in calculations of heat transfer. The other goal was to evaluate the distributions of the turbulent Prandtl number from the experimental data for flows with surface waves.

3.1. Flibe hydrodynamics (FliHy) experimental facility

The experiments were conducted using a water loop (Fig. 3) since the physical properties of the molten salts of interest do not substantially differ from those of water. The test section is a 4-m long, 40-cm wide inclined flume. The working fluid is injected continuously into the test section by two centrifugal pumps (up to 75 l/s), connected in parallel through an adjustable nozzle (3–50 mm height). The nozzle has a honeycomb and a secondary screen to reduce the inlet turbulence. The nozzle height is adjusted to provide an inlet flow thickness closer to the equilibrium one. This reduces the transition length significantly. The liquid is collected into a 1 m^3 tank at the bottom of the supporting frame. An infrared (IR) heater (30 cm × 30 cm, up to 60 kW/m^2) located 3 m down from the nozzle is used to heat the liquid from the side of the free surface. All measurements are conducted immediately after the heated area, where the mean flow is hydrodynamically fully developed. The measurements include IR images from the FLIR-600 IR camera, as well as the flow thickness versus time measured by the 10 MHz 3 mm V129-RM Panametrics ultrasound transducer. A more detailed description of the experimental facilities and approaches is given in [18].

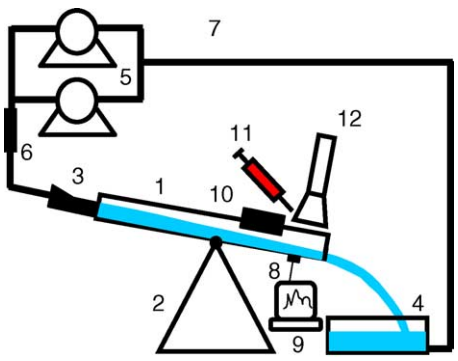

Fig. 3. Schematic diagram of experimental equipment: (1) inclined test-section, (2) frame, (3) nozzle, (4) tank, (5) two pumps, (6) flowmeter, (7) hoses, (8) ultrasound transducer, (9) PC, (10) IR heater, (11) dye injector, (12) IR camera.

The dimensionless flow parameters that characterize the flow are the Reynolds number ($Re = U_m h_m/\nu$), the Froude number ($Fr = U_m^2/gh_m$), and the Weber number ($We = U_m^2 \rho h_m/\sigma_T$). The parameters are built using the mean velocity, U_m, and the mean flow thickness, h_m, of the fully developed flow as the velocity scale and the length scale; σ_T is the surface tension. Another definition of the Froude number, $Fr_\perp = Fr/\cos\alpha$, which is built through the component of $\boldsymbol{g}$ normal to the flume bottom ($g_\perp = g\cos\alpha$, where α is the flume inclination angle), is also used. The experiments were conducted in the following range of the flow parameters, which meets the CLiFF flow conditions: $0.1^\circ \le \alpha \le 75^\circ$; $0.45\,\text{m/s} \le U_m \le 7.9\,\text{m/s}$; $0.005\,\text{m} \le h_m \le 0.022\,\text{m}$. The corresponding dimensionless numbers were changing in the following range: $10\,000 \le Re \le 51\,000$; $0.94 \le Fr \le 1250$; $0.94 \le Fr_\perp \le 4830$; $60 \le We \le 5230$. Note that the basic results in the present study have been obtained based on the experimental data within this particular range and thus their applicability should be restricted to this range.

3.2. Interpretation of the data with the "L–q" diagram

Numerous observations of free surface deformations have shown that key physical mechanisms are related to the stabilization effect of capillary tension and gravity forces against the disrupting effect due to the turbulence kinetic energy (e.g. [5]). In so-called "weak" turbulence, there is little or no surface disturbance. In this regime, once the bulk turbulence reaches the free surface, the turbulent fluctuations become predominantly parallel to the surface. A near-surface blockage layer is formed in which the scalar transport across the free surface is significantly reduced in comparison with the flow bulk. In contrast to weak turbulence, in "strong" turbulence, neither surface tension nor gravity can restrain the fluctuating eddies: the flow breaks up into drops. The absence of a sharp boundary between these two regimes also implies a transition region of marginal breaking that spans a substantial range of the flow parameters, in which different variations between a surface that is no longer smooth and one that is broken can also be observed.

A convenient way of characterization of the free surface is the "*L*–*q*" diagram (Fig. 4), recently suggested in [5]. Rather than using dimensionless parameters, this

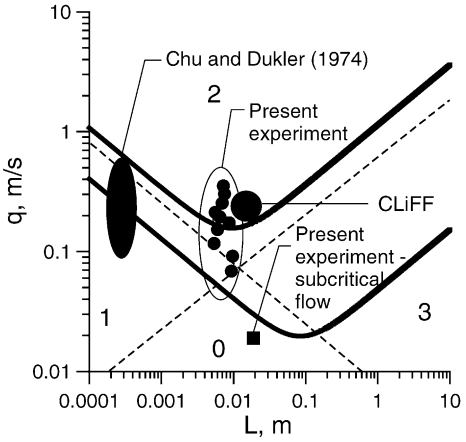

Fig. 4. *L*–*q* diagram adapted from [5] with the present experimental data, CLiFF parameters, and data for film flows [20,21]. Region 0 is weak turbulence. Region 1 is turbulence with surface tension dominant over gravity. Region 2 is strong turbulence. Region 3 is gravity-dominated turbulence. The area between the two solid lines represents transitional region of marginal breaking.

diagram operates with two-dimensional quantities, *L* and *q*, which are the length scale and the overall velocity of a typical turbulent element of fluid near the free surface. In the diagram, the (*L*, *q*)-plane is subdivided by the two dotted lines into four characteristic regions. In addition to the already mentioned weak and strong turbulence regions, the diagram shows two others with no surface disintegration, in which gravity or surface tension is a major factor, and the surface phenomena associated with gravity or capillary waves are correspondingly dominant. The area between the two solid lines represents the transitional region of marginal breaking. It should be noted that the diagram allows only qualitative conclusions on the regime in a given flow and does not provide any flow details. Detailed information should be based on experimental data or modeling.

The parameters corresponding to the CLiFF flows are plotted in the diagram with the friction velocity as *q*, and the flow thickness as *L*. In estimations of *q*, the MHD effects were taken into account by using the present K–ε model. In the CLiFF design, the liquid flows along a curved wall so that the effective force acting in the direction normal to the free surface consists of the gravity force and the centrifugal force. This was taken into account by introducing an effective acceleration, such that $g_{\text{eff}} = g_\perp + U_m^2/R$, where

R is the radius of curvature of the solid structural wall. The quantity g_{eff} should be considered as a parameter in Fig. 4. However, changing g_{eff} in a wide range does not affect significantly the position of the basic curves in the figure so that the qualitative description given by the diagram is still the same. This is why, the effect related to changes of g_{eff} has not been shown. As it can be seen, the CLiFF regimes run mostly into the transitional area from weak to strong turbulence, with about equal effect of gravity and surface tension. The flow parameters from the present experiments are also plotted in the same diagram representing an area that corresponds to the same flow regime. Thus, physical similarity between the experiment and the CLiFF-type flows has been established. The present experimental observations show large-amplitude waves but almost no splashing. Some insignificant drop formation was noticed at deep inclinations in almost vertical flows. Visual observations showed much more waviness at the surface as the flow rate and/or the inclination angle grew. Directly at the nozzle, the free surface is smooth; the surface waves grow in amplitude downstream reaching a quasi-saturation state over some distance (1–2 m) from the nozzle, which varies depending on the flow parameters.

3.3. Characterization of the fluctuating flow thickness

The fluctuating flow thickness was measured as a function of time at a given point within the fully developed flow section employing an ultrasound transducer. The statistical analysis performed on the experimental data is similar to that developed by Dukler and coworkers [19–21] for film flows. It included evaluation of the mean flow thickness and its standard deviation, probability density function, and power spectral density (PSD).

Each of the $h(t)$ curves (Fig. 5) is based on the subsequent measurements of the flow thickness taken with a time increment of 1 ms. The number of the measurements in one sample is limited by the hardware capabilities and usually consisted of 509 data points. The instrumental error in h is mostly contributed by the error in the ultrasound travelling time measured with the oscilloscope and was estimated as 100 μm. This error is insignificant in comparison with the mean flow thickness but it is not negligible in evaluations of the waviness parameter, which is defined here as the ratio of the standard deviation of the flow thickness to the mean thickness, σ/h_{m}. The water–air interface demonstrates irregular wave-type behavior with wave frequency and amplitude increasing with inclination angle. From the obtained PSD plots (Fig. 6), one can see a large peak at about 10–40 Hz, as well as a long "tail" of higher frequency modes. Therefore, both capillary and gravity waves are presented in the spectrum. As the inclination angle grows, the contribution of shorter waves becomes more significant, making the interface more irregular.

In Fig. 7, data for a waviness parameter are plotted as a function of $Fr_{\perp}$ using a semi-log scale. Since

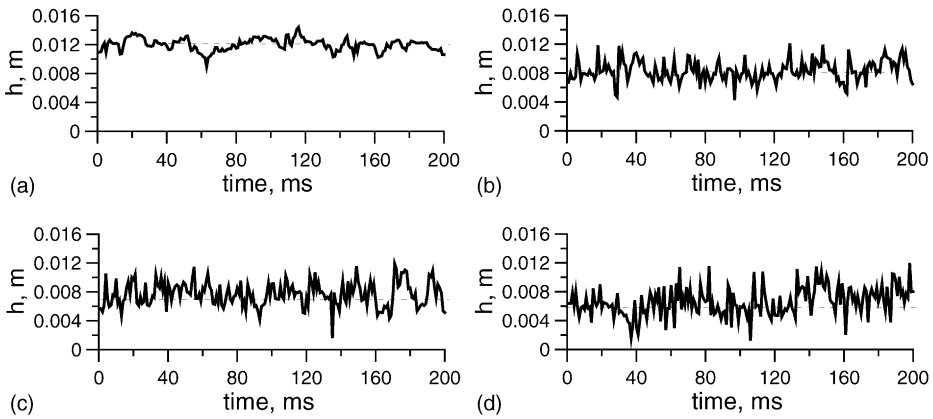

Fig. 5. Flow thickness vs. time measured with the ultrasound transducer: (a) $\alpha = 3.5^{\circ}$, $Re = 24\,250$, $Fr_{\perp} = 50$, $h_{\text{m}} = 0.012$ m, $\sigma = 0.0009$ m; (b) $\alpha = 30^{\circ}$, $Re = 37\,000$, $Fr_{\perp} = 260$, $h_{\text{m}} = 0.008$ m, $\sigma = 0.0014$ m; (c) $\alpha = 50^{\circ}$, $Re = 37\,750$, $Fr_{\perp} = 670$, $h_{\text{m}} = 0.007$ m, $\sigma = 0.0015$ m; (d) $\alpha = 75^{\circ}$, $Re = 37\,500$, $Fr_{\perp} = 2790$, $h_{\text{m}} = 0.0058$ m, $\sigma = 0.0016$ m.

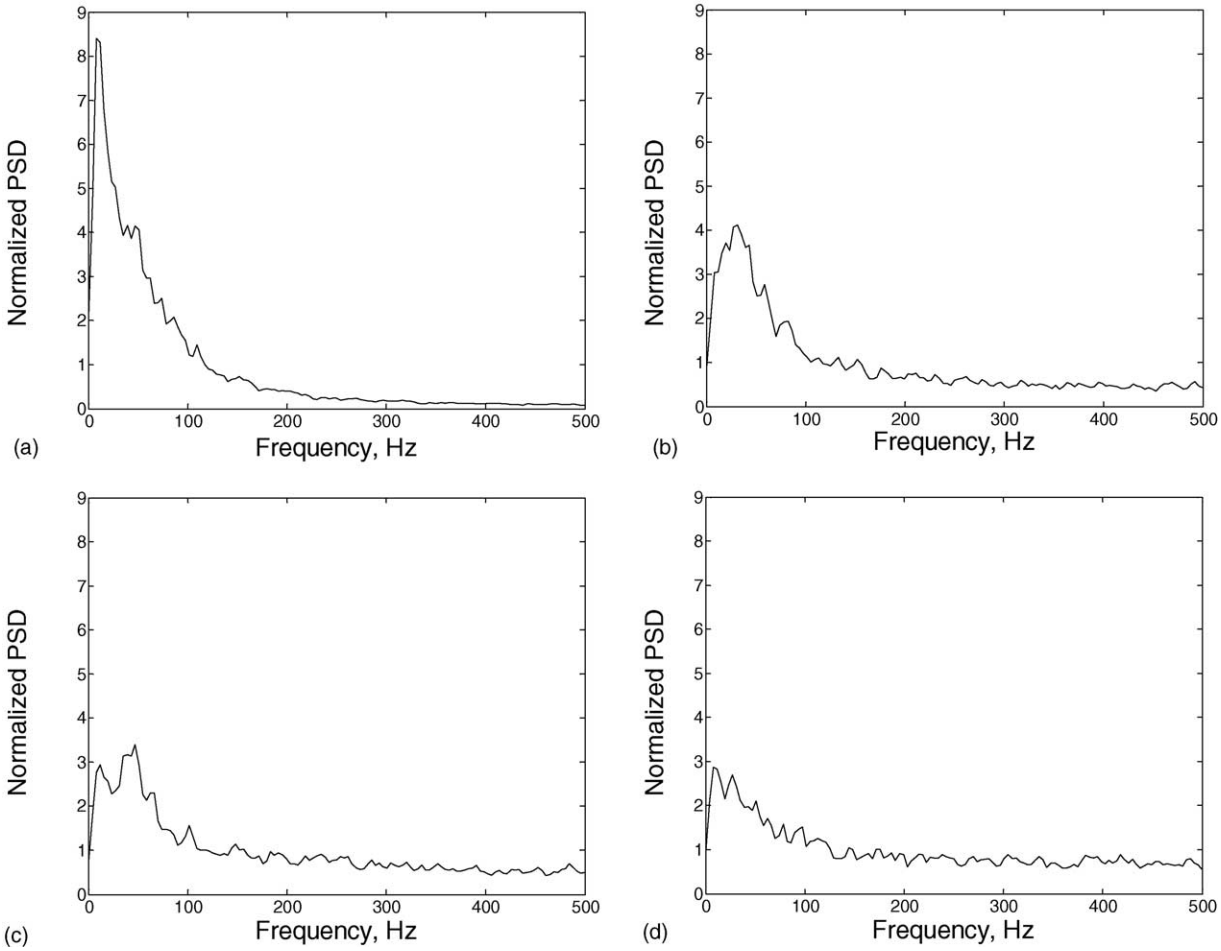

Fig. 6. Power spectral density (PSD): (a) $\alpha = 3.5^\circ$, $Re = 24\,250$, $Fr_\perp = 50$, $h_m = 0.012$ m, $\sigma = 0.0009$ m; (b) $\alpha = 30^\circ$, $Re = 37\,000$, $Fr_\perp = 260$, $h_m = 0.008$ m, $\sigma = 0.0014$ m; (c) $\alpha = 50^\circ$, $Re = 37\,750$, $Fr_\perp = 670$, $h_m = 0.007$ m, $\sigma = 0.0015$ m; (d) $\alpha = 75^\circ$, $Re = 37\,500$, $Fr_\perp = 2790$, $h_m = 0.0058$ m, $\sigma = 0.0016$ m.

this parameter is within 0.01–0.35, the waves observed should be classified as finite-amplitude waves. One can see that the effect of the velocity and the inclination angle on the waviness parameter is correlated very well using $Fr_\perp$ only. The best fit, which relates the waviness parameter to $Fr_\perp$, was found to be

$$\frac{\sigma}{h_m} = 5.11 \times 10^{-03}(\ln\ Fr_\perp)^2 - 2.60\times10^{-03}\ \ln\ Fr_\perp + 0.015. \quad (10)$$

The changes in PSD, such as a bigger fraction of higher frequency modes, and the amplitude growth with $Fr_\perp$ can be explained by reduction in the stabilizing action of gravity against the disturbing influence of turbulence at steeper inclinations. As the inclination angle grows, more and more turbulent elements from the flow bulk (smaller in size and with less energy) can reach and deform the free surface, resulting in more irregular interface behavior.

3.4. Predictions of the mean flow thickness with the K–ε model

The present experimental data were used to clarify the limitations of the standard K–ε model when applied to calculations of turbulent open channel flow with surface waves. The mean equations being solved

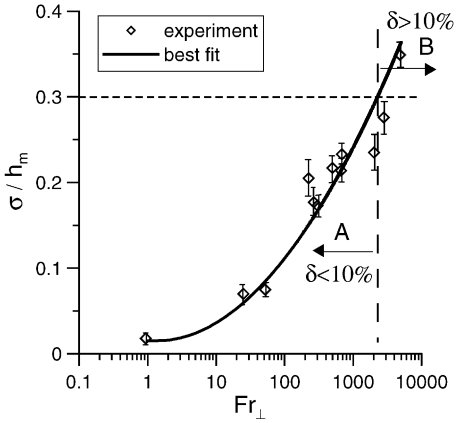

Fig. 7. The waviness parameter as a function of $Fr_\perp$. If σ/h_m is smaller than about 0.3 (area A), the K–ε predictions of the mean flow thickness are within 10%. At higher waviness (area B), the K–ε predictions are unsatisfactory.

are written in the Cartesian coordinates using the thin-shear-layer approximation with the x-axis in the main flow direction, the y-axis perpendicular to the flume bottom, and the coordinate origin located on the bottom in the inlet cross-section, as follows:

$$\frac{\partial U}{\partial t} + U\frac{\partial U}{\partial x} + V\frac{\partial U}{\partial y} = -g\cos(\alpha)\frac{\partial h}{\partial x} + g\sin(\alpha) + \frac{\partial}{\partial y}\left[(\nu + \nu_t)\frac{\partial U}{\partial y}\right], \quad (11)$$

$$\frac{\partial U}{\partial x} + \frac{\partial V}{\partial y} = 0, \quad (12)$$

$$\frac{\partial h}{\partial t} + U_s\frac{\partial h}{\partial x} = V_s. \quad (13)$$

Here, $U(t, x, y)$ and $V(t, x, y)$ are the mean velocity components, and $h(t, x)$ is the mean flow thickness. The subscript "s" denotes the free surface. Eqs. (11) and (12) are used to calculate the mean velocity. Eq. (13), the kinematic free surface condition, serves for calculating $h(t, x)$. The boundary conditions on the velocity components consist of a no-slip condition at the flume bottom and no-tangential stress at the free surface. The eddy viscosity, ν_t, entering Eq. (11) is calculated by the Kolmogorov–Prandtl expression. The equations for K and ε are based on those (2) and (4) but are taken here without the electromagnetic terms. Besides, the low-Reynolds number modification of these equations was used in the form proposed by Chien [22] to provide accurate predictions of the flow down to the flume bottom. The Hossain and Rodi boundary conditions (6) were employed as boundary conditions on K and ε at the free surface.

The equations were approximated with the finite-difference formulas using a stretched grid, which concentrates grid points near the flume bottom and the free surface. To provide for proper resolution in the bottom vicinity, the number of grids across the flow was varied between 50 and 200, depending on the turbulence Reynolds number, with the first grid point located between $y_+ = 0.1$ and $y_+ = 0.5$. The solution was sought as the steady state of a time-dependent problem, using a Blottner-type finite-difference method [23] with a height-function method as a technique for tracking the free surface [24].

The results of the calculations for the mean flow thickness, $h_{K-\varepsilon}$, within the fully developed flow section are summarized in Table 3 along with the ex-

Table 3
Comparison of the mean flow thickness calculated with the K–ε model ($h_{K-\varepsilon}$) and experimentally (h_m)

α (°)	U_m (m/s)	h_m (m)	σ (m)	σ/h_m (%)	Re	Fr	$Fr_\perp$	We	$h_{K-\varepsilon}$ (m)	δ (%)
0.1	0.452	0.0221	0.0004	1.8	10000	0.94	0.94	60	0.0232	4.9
3.5	1.45	0.0100	0.0007	7.0	14500	25	25	280	0.0097	3.0
3.5	2.03	0.0120	0.0009	7.5	24250	50	50	670	0.0126	5.0
30	2.91	0.0044	0.0009	20.5	12750	190	220	500	0.0046	4.5
30	3.90	0.0068	0.0012	17.7	26500	230	260	1400	0.0070	3.0
30	4.57	0.0081	0.0014	17.3	37000	260	300	2280	0.0086	6.2
50	3.71	0.0060	0.0013	21.7	26000	320	500	1120	0.0060	0.0
50	5.40	0.0070	0.0015	21.4	37750	430	670	2760	0.0075	7.1
50	6.01	0.0084	0.0021	23.3	50500	440	680	4100	0.0090	7.1
75	5.10	0.0051	0.0012	23.5	26000	520	2010	1790	0.0056	9.8
75	6.47	0.0058	0.0016	27.6	37500	720	2790	3280	0.0069	19.0
75	7.94	0.0063	0.0022	34.9	50000	1250	4830	5230	0.0083	31.7

perimental parameters and the mean flow thickness measured experimentally. The parameter $\delta = (h_{K-\varepsilon} - h_m)/h_m$ in the table characterizes the difference between the experimental and computed data.

The comparison of the mean flow thickness gives a range of applicability of the model. If the waviness is relatively small, the coincidence is good enough. However, the discrepancy grows with the waviness parameter. In high waviness regimes, the K–ε model always overestimates the mean flow thickness. At high σ/h_m, the model gives inaccurate predictions. A level of 10% difference has been chosen as a conventional limit of the model applicability. The critical value of the waviness parameter that corresponds to this level was found to be 0.3 (Fig. 7). In accordance with formula (10), it corresponds to $Fr_\perp \approx 2000$. This is also the level of waviness where the free surface disturbances can extend all the way down to the bottom wall of the flow.

3.5. Predictions of the surface temperature and evaluations of Pr_t for wavy flows

In the context of the present study, the heat transfer problem can be described by the averaged energy equation

$$\rho C_p \left(\frac{\partial T}{\partial t} + U\frac{\partial T}{\partial x} + V\frac{\partial T}{\partial y} \right) = \frac{\partial}{\partial y}\left(k_{\text{eff}} \frac{\partial T}{\partial y} \right) \qquad (14)$$

and the boundary condition at the free surface that simulates a heat flux, q'', applied to the surface within the heated area. Here k_{eff} is the effective thermal conductivity coefficient that stands for both the molecular and turbulent heat transport ($k_{\text{eff}} = k + k_t$). $T(t, x, y)$ is the mean temperature in the liquid, and ρ and C_p are the fluid mass density and specific heat. Accordingly to (1b), the turbulent component of the effective thermal conductivity can be expressed in the following way:

$$\frac{k_t}{k} = \frac{\nu_t}{\nu}\frac{Pr}{Pr_t}.$$

Once the distribution of Pr_t is known, the temperature field in the liquid can be calculated by solving Eq. (14) with U, V and ν_t calculated by the hydrodynamic code as input data. For subcritical flows ($Fr_\perp < 1$), a Pr_t distribution as a function of depth was evaluated in [7] based on the experimental data for the eddy diffusivity for heat [4]. The best-fit was found as

$$Pr_t = 0.7\left[1 + \exp\left\{A\left(\frac{y}{h_m} - 0.89\right)\right\}\right], \quad A = 37. \qquad (15)$$

The present evaluations of Pr_t for supercritical flows ($Fr_\perp > 1$) that exhibit a wave behavior also adopt Eq. (15), but unlike the direct approach in [7], are based on an indirect method that adjusts the parameter A through matching the experimentally measured surface temperatures with those calculated with the present model. The heat transfer code implements the same finite-difference formulation as described in Section 3.4.

A typical thermal image of the free surface, immediately after the flow exits the lower heater edge region, taken with the IR camera, is shown in Fig. 8. The temperature field of the free surface is essentially non-uniform and time varying. One can see "hotter" and "cooler" spots in the form of streaks elongated in the flow direction, that appear due to the significant interface irregularities. The temperature non-uniformity seen in the image can serve as an indirect confirmation of the overturning waves and surface renewal phenomena. To obtain the mean temperature distribution along the main flow direction, the thermal images were averaged in the spanwise direction over the 20 cm strip and in time, for a period of approximately 10 s. If these data are plotted in a dimensional form in the same figure, the experimental points are mixed making their comparison difficult. To present the data in a compa-

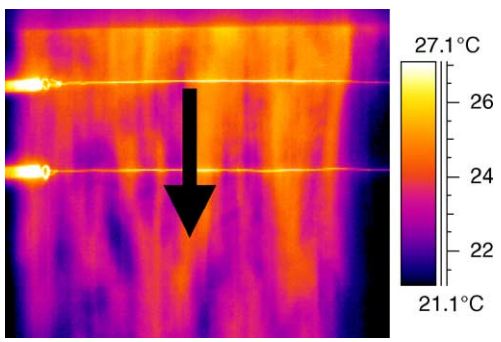

Fig. 8. Typical snapshot of the water surface with the IR camera. The arrow shows the flow direction. The heat flux is applied to the free surface. Two thin strips in the spanwise direction are the thermal images of heated wires located above the surface, which are used as a length scale. The wires are 5 cm apart.

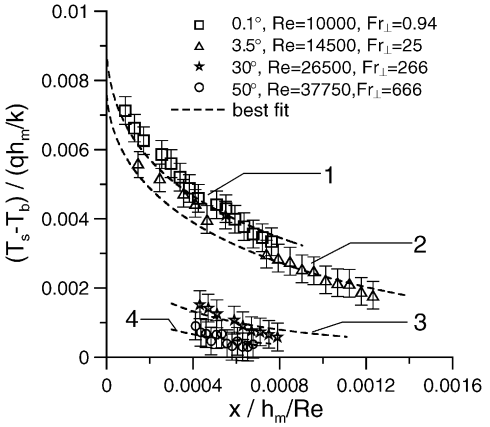

Fig. 9. Dimensionless mean surface temperature profiles measured in the experiment and calculated. The parameter A in formula for Pr_t has been evaluated as follows: (1) A = 37.9; (2) A = 35.3; (3) A = 29.0; (4) A = 27.1.

rable form, it is reasonable to introduce scales, such as $q''h_m/k$ as a temperature scale and h_m/Re as a length scale. The choice of the scales is based on the dimensionless form of the energy equation. Such dimensionless temperature profiles after averaging are shown in Fig. 9. Once the liquid leaves the heated area, the mean surface temperature drops fast due to transport of heat into the flow bulk. The separation of temperature curves in the figure is explained by increasing the cooling rate in the free surface vicinity as the waviness grows. In terms of the K–ε model adopted in the present study, increasing the coolant rate means lower values of Pr_t. The improvement of heat transfer is directly related to better mixing of liquid at the free surface due to relatively short waves with the characteristic dimension comparable with the mean flow thickness or smaller. As it was shown, the contribution of such waves into the wave spectrum grows with $Fr_\perp$.

First, to verify the present approach of evaluating Pr_t, the analysis was performed on subcritical flow data (first row in Table 3). The parameter A was found to be 37.9. This is rather close to 37, the value evaluated in [7]. The discrepancy is insignificant and can be explained by different experimental conditions and the absence of measurements in the immediate vicinity of the free surface in [4]. The evaluation of Pr_t in a supercritical flow was then performed using the same approach across the range of the flow parameters for which the model was shown to be applicable, i.e. $\alpha \leq 50^\circ$ or $Fr_\perp < 700$. Typical examples of matching the experimental data with the calculations by adjusting the parameter A are also shown in Fig. 9. Finally, the following approximations are recommended for calculations with the K–ε model:

$$A = \begin{cases} 38 - 0.05\,Fr_\perp & Fr_\perp = 0\text{–}100, \\ 34 - 0.01\,Fr_\perp & Fr_\perp = 100\text{–}700. \end{cases} \quad (16)$$

Accordingly to (16), A drops from 38 to 27 as $Fr_\perp$ grows from 0 to 700.

4. Examples of application of the model to the CLiFF flows and heat transfer

The examples include hydrodynamic and heat transfer calculations for Flinabe flows over the reactor outboard First Wall and divertor using parameters relevant to the CLiFF design. The liquid is injected at the chamber top, flows down along the curved reactor wall under the gravity effect, and then is extracted somehow at the bottom of the chamber. The flow is affected by a strong (B_0 = 10 T) toroidal reactor magnetic field and exposed to a high heat flux from the reactor plasma. The liquid layer adheres to the curved wall by means of its centrifugal acceleration, U_m^2/R, where R is the radius of curvature of the flow streamlines. The flow is supposed to be continuous in the toroidal direction without subdividing it into sections. The layer is utilized at the bottom of the reactor as an integrated liquid surface divertor.

The present K–ε model was used to calculate the downstream changes of the flow. First, different flow regimes were calculated for thick and thin flows (Fig. 10). The thick flows experience significant gravitational contraction. The MHD effects on the mean flow are negligible because of a low electrical conductivity of Flinabe and also due to the fact that any solid walls perpendicular to the toroidal magnetic field are not present. At the same time, thin flows demonstrate more uniform distributions over almost the entire flow length. One of the cases calculated, with the inlet velocity, U_0, of 10 m/s and the inlet flow thickness, h_0, of 2.3 cm, demonstrates no variations. This flow regime has been chosen as a reference case and the same flow parameters were also used in the heat transfer calculations.

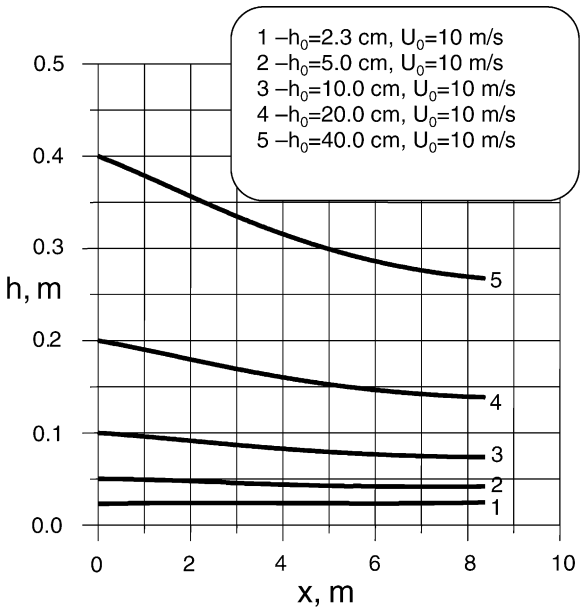

Fig. 10. Downstream changes of the flow thickness for thick and thin flows calculated with the K–ε model.

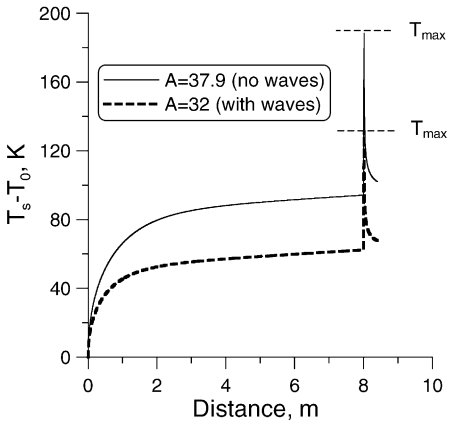

Fig. 11. Surface temperature rise over the First Wall/divertor area.

The surface heat flux distribution adopted in the present calculations underlines the basic features of the real heat flux distribution in the outboard region by using a step-type function. The heat flux of 1.4 MW/m^2 is applied over the First Wall area, jumps to 12 MW/m^2 over a 2-cm section within the divertor region, and then drops down to 1.4 MW/m^2 again. The flow scheme presently considered assumes a continuous flow over the whole area. Another scheme that realizes hydrodynamic mixing before the liquid enters the divertor section is proposed in [25] using a so-called "deflector". Mixing the liquid results in the surface temperature drop immediately after the point of mixing down to the bulk temperature. Mixing may be necessary if the surface temperature within the First Wall section goes too high, above the acceptable limit. When evaluating the waviness effect, the parameter $Fr_\perp$ was estimated by including the centrifugal acceleration, U_m^2/R, into g_{eff}. Corresponding value of the parameter A entering the expression for the turbulent Prandtl number was found to be 32. The results of heat transfer calculations are shown in Fig. 11 in the form of the surface temperature rise ($T_s - T_0$) versus the distance along the reactor wall, where T_s is the surface temperature and T_0 is the inlet temperature. The figure also demonstrates the effect of waves. These calculations do not include bulk heating due to neutrons, since it almost does not affect the surface temperature and has a primary impact on the bulk temperature. The results calculated here and other heat transfer data are also analyzed in [2] from the point of view of the "design window". Some extra details related to heat transfer, which were not fully analyzed in the present paper, are also discussed in [2] and partially in [25].

5. Novel approaches for heat transfer enhancement

Although the surface waves arising of natural reasons are fairly effective from the point of view of heat transfer enhancement, additional mixing of liquid near the free surface can be a favorable factor if the natural waviness is not high enough or surface temperature is still above the allowable limit. As previous considerations show, better conditions for heat transfer can be provided by surface waves whose length scale is comparable or smaller than the flow thickness. Two schemes of generating such waves were designed (Fig. 12) and tested using the present experimental facilities. First, overlays with triangular riblets oriented in the flow direction were manufactured from acrylic to fit on the flat back-wall of the plane test-section. Second, heat transfer promoters in the form of cylinders made of a copper wire located across the stream were mounted on the back-wall surface to form a periodi-

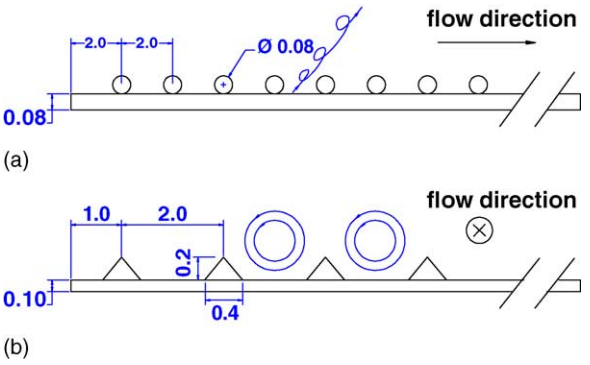

Fig. 12. Schematic diagram for heat transfer promoters: cross cylinders (a); longitudinal triangular riblets (b). Dimensions in cm.

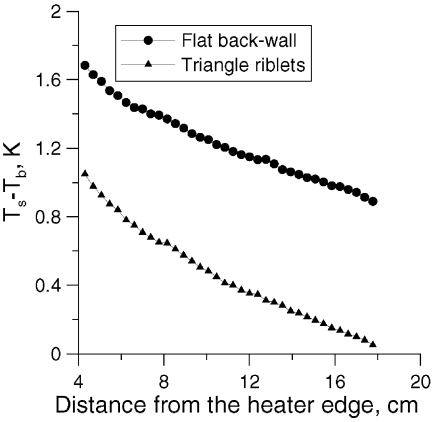

Fig. 14. Mean free surface temperature as a function of distance from the heater edge for flat and modified (triangle riblets) back-wall: α = 3.5°; *Re* = 14 500; *Fr* = 25.

cal array of obstacles. In both cases, the dimensions of the promoters were chosen to be small enough so that the promoters were fully submerged in the liquid, and splashing of the liquid was not observed. In both cases, the flow structures at the free surface are visually different from those in the flow without heat transfer promoters, both in size and to some degree in shape and orientation (Fig. 13). These structures are of a cell type and arise as a result of interaction of bulk turbulence with the free surface. A tendency towards forming smaller structures at the surface is especially clear in case of the cross cylinders.

At present, heat transfer measurements are accomplished for the case of longitudinal riblets. A comparison for the mean free surface temperature measured with and without promoters is shown in Fig. 14. The results presented are for α = 3.5°. Unlike flows at steeper inclinations, this case does not demonstrate much surface waviness, and hence the effect of the promoters on heat transfer can be observed in an almost "pure" form. One can see distinctive reduction in the surface temperature when the heat promoters are used as well as higher cooling rate. More experimental results are presented in Table 4, which gives a summary of multiple measurements for different flow conditions corresponding to different inclination angles and flow velocities. Each

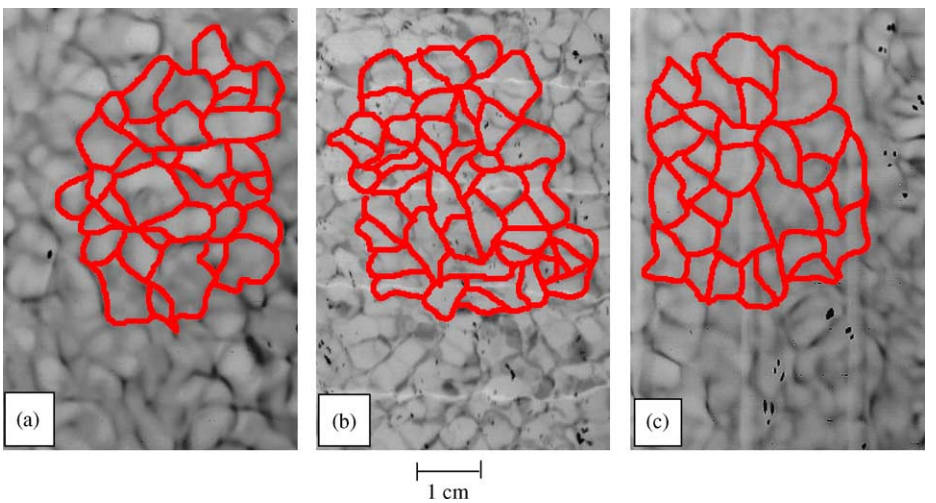

Fig. 13. Photographs of the wave structures at the surface of inclined water flows with and without heat transfer promoters: (a) flat back-wall; (b) with cross cylinders; (c) with longitudinal ribs. All pictures are taken at the same *Re* = 14 500 and α = 3.5°.

Table 4
Mean surface temperature difference with and without heat transfer promoters (triangular riblets)

α (°)	*Re*	*Fr*	$(\Delta T)_1$, no promoters (K)	$(\Delta T)_2$, with promoters (K)	$\frac{\Delta T_1 - \Delta T_2}{\Delta T_2}$ (%)
0.1	10000	0.94	3.47	2.67	30
3.5	14500	25	1.53	1.05	46
3.5	24250	50	1.68	1.03	63
50	26000	320	2.74	2.17	26
75	37500	720	2.71	2.30	18

$\Delta T = T_s - T_b$, where T_s is the mean surface temperature measured 4 cm downstream of the heater edge and T_b is the bulk temperature.

couple of measurements performed for the smooth and modified back-wall was conducted at the same heat load. Thus, direct comparisons of the heat transfer rate between these two cases are possible. The data in the table are presented in terms of the temperature difference, $\Delta T = T_s - T_b$. The surface temperature, T_s, was measured 4 cm downstream the heater edge using the IR camera. Since the variations of the bulk temperature with the longitudinal distance are very small, the thermocouple that measured the bulk temperature was positioned outside the IR camera observation window to avoid possible effects on the measurements of the surface temperature. One can see that for all the inclinations and velocities, the modified back-wall flows demonstrate better heat transfer rate. This can be explained by generating additional vortical structures and therefore better fluid mixing in the near-surface region. However, this tendency also demonstrates a complex dependency on both the inclination angle and velocity. First, the temperature difference grows with the inclination angle, reaches its maximum, and then goes down at steeper inclinations. These observations allow for some conclusions on the role of natural waves in comparison with artificially generated vortical structures. At shallow inclinations, when the natural waviness is small, the effect of heat transfer improvement by promoters is significant. At higher waviness corresponding to deeper inclinations, the overall heat transfer rate is mostly contributed by natural waves. These conclusions are qualitative yet since systematical measurements have not been conducted.

6. Direct numerical simulation of free falling films

A turbulent free falling film is a typical example of open surface flows, in which free surface is agitated by a large number of different waves that demonstrate irregular behavior both in space and time. Even now, direct computer modeling of such flows encounters many technical problems related to the need for proper resolution of turbulence scales as well as a proper method for tracking the interface. Here, we present some first test calculations for the free falling films using a DNS technique.

The main goal of this research is a numerical investigation (through DNS) of turbulent open channel flows under conditions relevant to molten salt flows in a fusion reactor. The data obtained can be used at next stages to improve quality of engineering mathematical models of turbulence, such as the K–ε model applied in the present study. At present, the model utilizes a relatively simple set of flow conditions including flat geometry, no interfacial heat/mass transfer and no MHD effects. A stable numerical method based on a finite difference approach developed by Zang et al. [27] has been extended to treat flows with a free surface. This method is adopted from the projection method by Chorin [28] and the level-set method with reinitialization by Sussman et al. [29] for interface tracking. An important step in solving the Navier–Stokes equations by this method is to solve a Poisson pressure equation. This problem was treated with the BiCG-Stab method [30] and incomplete lower–upper factorization preconditioner (ILU). This projection step is crucial to maintaining a divergence-free field, and takes most of the computation time when dealing with high fluid density ratios. Hence, it is quite important to put great effort into the optimization of the solution method for the Poisson pressure equation for reaching sufficiently high Reynolds numbers relevant to flows in fusion applications.

Two different cases were calculated. The first calculation was performed at low Reynolds number (Re = 30), and the second one at Re = 240. The simulations

used periodic boundary conditions in the streamwise and spanwise directions and no-slip condition in the third direction at the solid wall. The periodic conditions in the streamwise direction was chosen so that a long evolution of the film flow can be studied with relatively high accuracy by using about 200 gird points per solitary wavelength (λ). The computational domain used was $4\lambda \times 2\lambda \times 2.2h$ (streamwise × spanwise × wall normal) where h is the film thickness. By doing this it was possible to simulate the flow behavior as if the simulation had been performed with inflow/outflow boundary conditions. In these simulations, the fluid properties are that of water for the liquid phase and air for the gas phase.

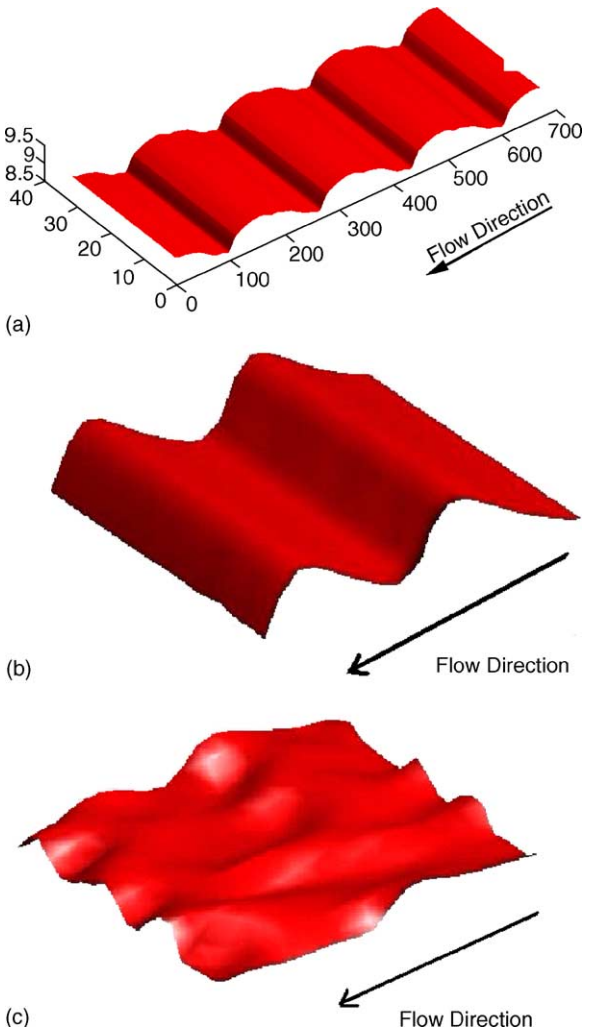

Fig. 15. Free surface deformations calculated by DNS for a free falling film flow: (a) $Re = 30$; (b) $Re = 240$ at $t = 0.2$ s; (c) $Re = 240$ at $t = 0.56$ s.

Although the computations performed are not in the turbulence regime yet, the free surface behavior is in a qualitative agreement with the experimental data presently available. The results calculated at $Re = 30$ (Fig. 15a) agree very well with those by Kapitza [31] that illustrate two-dimensional waves at low Re. The results at higher Re (Fig. 15b and c) are showed for the half of the computational domain of two initial wavelengths. Fig. 15b shows steep wave fronts growing from a small two-dimensional initial perturbation after 0.2 s. Fig. 15c shows the transition towards three-dimensional waves after 0.56 s. The present results are in a qualitative agreement with experimental data obtained in [32]. It is important to note that the flow is quite unsteady at that Re number and that Fig. 15c illustrates a well resolved film which shape has not qualitatively and statistically evolved for 0.2 s.

7. Concluding remarks

The major part of the present study is adjustment of the K–ε model for MHD free surface flows and the supporting experiments. The effect of a magnetic field was included through additional electromagnetic terms that stand for the Joule dissipation, and then the model was carefully adjusted by using known experimental data for MHD duct flows. The model is applicable to many flows with and without MHD effects, but fails to predict accurately supercritical flows with high waviness that occur when the surface waves penetrate all the way down to the solid wall. Comparisons of the calculations with experimental data show its range of applicability, which can be characterized with $Fr_\perp$. If $Fr_\perp < 2000$, the predictions of the mean flow thickness are within 10% accuracy of the experimental data. In terms of the average wave amplitude, the range of applicability of the model varies widely from subcritical flows, with no waves to those supercritical with the waviness parameter of 0.3. However, the model is inaccurate, if the surface waviness is sufficiently high ($Fr_\perp > 2000$ or $\sigma/h_m > 0.3$). Ways of extending the model performance can be shortly described as follows. First, the free surface boundary conditions implemented in the present model should be replaced

with different conditions more suitable for high waviness flows [33]. Second, extra terms in the form of an additional pressure gradient that stands for dynamical effects due to vertical accelerations should be implemented in the momentum equation. Some extra terms in the equation for K will be needed to take into account the effects of energy exchange between the turbulent motion in the flow bulk and the wave modes at the free surface. Third, in situations, when the surface disturbances penetrate all the way down to the bottom wall of the flow, the classic models for the turbulent boundary layer are most likely not applicable. This may require a modification of the low Reynolds number model presently adopted. All these changes will require a sufficient amount of experimental and theoretical work including efforts on development of turbulence closures and readjustment of the model coefficients. However, high waviness regimes most likely do not occur in the CLiFF design based on estimations of $Fr_\perp$ calculated from $g_{\text{eff}} = g_\perp + U_{\text{m}}^2/R$. Uncertainties stem from the unknown degree of the magnetic field effect on the surface waves.

The experiments conducted have revealed a key role of $Fr_\perp$. A qualitative description of the processes at a free surface in open channel flows considered in the present study can be summarized as follows. As $Fr_\perp$ grows, both the free surface and heat transfer rate experience significant changes. An increase in $Fr_\perp$ as the inclination angle grows results in a reduction of the stabilizing effect of gravity against the disturbing effect of turbulence. More and more turbulent structures from the flow bulk reach and disturb the free surface. These disturbances, along with the inherent surface instability, lead to complex wave-type phenomena with both capillary and gravity waves existing at the surface. The gravity waves carry a significant flow rate through the near-surface area, while the capillary-type waves (with wavelengths comparable to the flow thickness and shorter) are mostly responsible for the changes in interfacial heat transport. The effect of $Fr_\perp$ on the wave amplitude in the range of flow parameters presently employed is approximated very well by Eq. (10). The effect on spectral characteristics lies in shifting towards shorter disturbances as $Fr_\perp$ grows. Both these effects result in better heat transfer conditions through mitigating the blockage effect in the near-surface region. The near-surface turbulent Prandtl number distributions have been evaluated as a function of $Fr_\perp$ for $Fr_\perp < 700$. These distributions are given by Eqs. (15) and (16). Using these distributions along with the equations for K and ε, mean flow equations, and energy equation allows for thermofluid calculations of molten salt flows in the fusion reactor environment.

Novel techniques for heat transfer enhancement by using modifications of the wall topology in the form of longitudinal or cross obstacles have been proposed. The experimental results presented in the paper show that using these heat transfer promoters may result in a significant enhancement of heat transfer through generating additional vortical structures whose characteristic size is comparable with the mean flow thickness or even smaller. However, further studies are needed to quantify these phenomena and implement corresponding mechanisms in theoretical models.

Similar to other RANS models, the K–ε model cannot predict fluctuations. A step forward is using a DNS technique. Examples of application DNS to free surface flows are also given in the paper. Unfortunately, the effectiveness of the numerical method currently used is not high enough to perform calculations at Reynolds numbers relevant to fusion applications. However, calculations performed at lower Reynolds number demonstrate correct flow features including transition from 2D to 3D surface waves as the Reynolds number grows. Further progress towards higher Re calculations is expected through significant acceleration of the computer code. At present, implementation of faster spectral methods instead of finite-difference techniques is under development.

References

[1] M.A. Abdou, The APEX TEAM, On the exploration of innovative concepts for fusion chamber technology, Fusion Eng. Des. 54 (2001) 181–247.
[2] R. Nygren, et al., A fusion reactor design with a liquid first wall and divertor, Fusion Eng. Des., APEX Special Issue (2004).
[3] S. Komori, H. Ueda, F. Ogino, T. Mizushima, Turbulence structure and transport mechanism at the free surface in an open channel flow, Int. J. Heat Mass Transf. 25 (1982) 513–521.
[4] H. Ueda, R. Moller, S. Komori, T. Mizushina, Eddy diffusivity near the free surface of open channel flow, Int. J. Heat Mass Transf. 20 (1977) 1127–1136.
[5] M. Brocchini, D.H. Peregrine, The dynamics of strong turbulence at free surfaces. Part 1. Description, J. Fluid Mech. 449 (2001) 225–254.
[6] H. Branover, Magnetohydrodynamic Flows in Ducts, Willey, New York, Toronto, 1978.

[7] S. Smolentsev, M. Abdou, N. Morley, A. Ying, T. Kunugi, Application of the *K*–epsilon model to open channel flows in a magnetic field, Int. J. Eng. Sci. 40 (2002) 693–711.
[8] B. Freeze, S. Smolentsev, N. Morley, M. Abdou, Characterization of the effect of Froude number on surface waves and heat transfer in inclined turbulent open channel water flows, Int. J. Heat Mass Transf. (2003).
[9] D.C.Wilcox, Turbulence Modeling for CFD, 2nd ed., DCW Industries, 1988, p. 540.
[10] W. Rodi, Turbulence models and their application in hydraulics: a state of the art review, International Association for Hydraulic Research, Delft, The Netherlands, 1984, p. 104.
[11] S.B. Pope, Turbulent Flows, University Press, Cambridge, 2000.
[12] K. Kitamura, M. Hirata, Turbulent heat and momentum transfer for electrically conducting fluid flowing in two-dimensional channel under transverse magnetic field, in: Proceedings of the 6th International Heat Transfer Conference, Toronto, Canada, August 7–11, 1978, pp. 159–164.
[13] M. Takahashi, A. Inoue, M. Aritomi, M. Matsuzaki, Numerical analysis for laminar and turbulent liquid-metal flow, Fusion Eng. Des. 8 (1989) 249–256.
[14] S. Satake, T. Kunugi, S. Smolentsev, Advances in direct numerical simulation for MHD modelling of free-surface flows, Fusion Eng. Des. 61–62 (2002) 95–102.
[15] H.-C. Ji, R.A. Gardner, Numerical analysis of turbulent pipe flow in a transverse magnetic field, Int. J. Heat Mass Transf. 40 (1997) 1839–1851.
[16] G.G. Branover, A.S. Vasil'ev, Yu.M. Gel'fgat, E.V. Shcherbinin, Turbulent flow in a plane perpendicular to a magnetic field, Magnetohydrodynamics 4 (1966) 46–49.
[17] E.C. Brouillette, P.S. Lykoudis, Magneto-fluid-mechanic channel flow. I. Experiment, Phys. Fluids 10 (1967) 995–1001.
[18] B. Freeze, Ph. D. Dissertation, UCLA, 2003.
[19] A.S. Telles, A.E. Dukler, Statistical characteristics of thin, vertical, wavy, liquid films, Ind. Eng. Chem. Fundam. 9 (1970) 412–421.
[20] K.J. Chu, A.E. Dukler, Statistical characteristics of thin, wavy films. Part II. Studies of the substrate and its wave structure, AIChE J. 20 (1974) 695–706.
[21] K.J. Chu, A.E. Dukler, Statistical characteristics of thin, wavy films. Part III. Structure of the large waves and their resistance to gas flow, AIChE J. 21 (1975) 583–593.
[22] K.Y. Chien, Predictions of channel and boundary layer flows with a low-Reynolds number turbulence model, AIAA J. 20 (1982) 33–38.
[23] F.G. Blottner, Variable grid scheme applied to turbulent boundary layers, Comput. Meth. Appl. Mech. Eng. 4 (1974) 179–194.
[24] B.D. Nichols, C.W. Hirt, Calculating three-dimensional free surface flows in the vicinity of submerged and exposed structures, J. Comp. Phys. 12 (1973) 234–246.
[25] R. Nygren, et al., Design integration of liquid surface divertor, Fusion Eng. Des., APEX Special Issue (2004).
[26] Y. Yamamoto, T. Kunugi, A. Serizawa, Turbulence statistics and scalar transport in an open-channel flow, J. Turbulence JOT2 (2001) 010.
[27] Y. Zang, R.L. Street, J.R. Koseff, A non-staggered grid, fractional step method for time-dependent incompressible Navier–Stokes equations in curvilinear coordinates, J. Comp. Phys. 114 (1994) 18–33.
[28] A.J. Chorin, Numerical solution of the Navier–Stokes equations, Math. Comput. 22 (1968) 745–762.
[29] M. Sussman, P. Smereka, S. Osher, A level set approach for computing solutions to incompressible two-phase flow, J. Comp. Phys. 114 (1994) 146–154.
[30] H.A. Van der Vorst, Bi-CGSTAB: a fast and smoothly converging variant of Bi-CG for the solution of nonsymmetric linear systems, SIAM J. Sci. Stat. Comput. 13 (1992) 631–644.
[31] P.L. Kapitza, Experimental study of ondulatory flow conditions, in: D. Ter Haar (Ed.), Collected Papers of P.L. Kapitza, Pergamon Press, Oxford, 1964.
[32] P. Adomeit, U. Renz, Hydrodynamics of three-dimensional waves in laminar falling films, Int. J. Multiphase Flow. 26 (2000) 1183–1208.
[33] M. Brocchini, Free surface boundary conditions at a bubbly/weakly splashing air–water interface, Phys. Fluids 14 (2002) 1834–1840.